RSC Advances

PAPER

View Article Online
View Journal | View Issue

Cite this: *RSC Adv.*, 2025, **15**, 48937

Received 20th August 2025
Accepted 12th November 2025

DOI: 10.1039/d5ra06191a

rsc.li/rsc-advances

A hollow mesoporous magnetic silica-based nanocomposite supported on copper ferrite functionalized with phosphomolybdic acid as a nanocatalyst for the synthesis of 1,4-dihydropyridines

Mahla Dadaei and Hossein Naeimi *

Porous nanomaterials are substances characterized by structures containing holes. Due to their extensive porous surface areas, these materials exhibit high reactivity and are of use as catalysts. In this study, a hollow nanocatalyst of magnetic mesoporous copper ferrite functionalized with phosphomolybdic acid was prepared and characterized by XRD, SEM, EDX, FT-IR, and VSM techniques that are each separately discussed in the text. This catalyst was used in a reaction to synthesize 1,4-dihydropyridine derivatives through a three-component reaction of barbituric acid, ammonium acetate and various benzaldehyde derivatives. After purification of the products with ethanol, the products were identified using physical and spectroscopic data, such as melting point, FT-IR, and ^{1}H NMR. Also, this catalyst can be recovered and reused five times without losing its catalytic activity.

Introduction

Recently, magnetic nanoparticles have attracted significant attention from researchers due to their desirable features that enable their application in various scientific fields such as nanocatalysts, biopharmaceuticals,[1] magnetic resonance imaging (MRI),[2] magnetic particle imaging,[3] and data storage.[4] To date, various methods have been proposed for the synthesis of magnetic nanoparticles.[5]

When synthesizing magnetic nanoparticles, several important factors must be considered, such as the intrinsic magnetic properties, size and structure of the nanoparticles, surface coating and surface charge, stability in aqueous environments, as well as their non-toxicity. Using an ideal synthetic method, it is possible to appropriately control the size, shape, surface coating, and colloidal stability of magnetic nanoparticles. Among nanoscale magnetic materials, in addition to iron oxide, other iron-containing compounds also exhibit the magnetic properties required for biomedical applications. Ferrites are particularly valuable due to their ability to have their physicochemical properties controlled by an external magnetic field, making them highly suitable for other applications such as.[6,7] Nanoparticles designed for such purposes must exhibit low toxicity, high structural stability, and significant superparamagnetic behaviour at room temperature (RT). Among magnetic nanoparticles, spinel ferrites (SFs) are represented by the chemical formula MFe_2O_4, where M refers to a divalent cation such as Co, Cu, Fe, Mn, or Ni. Among SFs, particularly cobalt ferrite ($CoFe_2O_4$) and copper ferrite ($CuFe_2O_4$) have attracted significant attention due to their high coercivity, notable mechanical and chemical stability, and pronounced magnetocrystalline anisotropy, making them important from physical, chemical, and biomedical perspectives.[8–10]

Depending on the synthesis technique and calcination temperature, $CuFe_2O_4$ can crystallize in two crystal structures, namely cubic spinel and tetragonal. Common nanoparticle synthesis methods include hydrothermal,[11] sonochemical,[12] sol–gel,[13] citrate–nitrate,[14,15] co-precipitation[16,17] and solid-state[18] techniques. Recently, $CuFe_2O_4$ materials with various morphologies have been studied and reported. To date, $CuFe_2O_4$ spinel has been extensively utilized in diverse fields, including heterogeneous catalysis,[6,7] photocatalysis,[6] and energy storage[11] and as an anode material for batteries.[13]

Porous materials consist of a network of regular and irregular pores or cavities, which possess a large surface area and controllable pore size.[19,20] Mesoporous materials are widely employed as drug carriers due to their exceptional properties, including a high surface area-to-volume ratio, tunable particle size,[21] and excellent biocompatibility and biodegradability.[22]

In recent years, research on the synthesis of mesoporous silica nanoparticles for biomedical applications has dramatically increased, leading to significant advancements in this field. In 2001, MCM-41 was first introduced as a drug delivery system; subsequently, other mesoporous silica frameworks

---

Department of Organic Chemistry, Faculty of Chemistry, University of Kashan, Kashan, 87317, Islamic Republic of Iran. E-mail: naeimi@kashanu.ac.ir; Tel: +98 3155912397; +98 3155912388

such as SBA-15 and MCM-48 have been identified and extensively studied as carriers for drug delivery and controlled release systems.[23,24] Mesoporous silica nanoparticles are now commonly utilized in medicine for the targeted delivery of therapeutic agents and bioactive compounds within the body.

Solid catalysts based on ordered mesoporous materials have garnered considerable attention due to their uniform and well-defined distribution of active catalytic sites on the substrate surface.[25] These materials exhibit a relatively homogeneous and controllable density of catalytically active centres, which contributes to the consistent reproducibility of synthesized catalysts.[26,27] Moreover, the presence of ordered mesopores significantly alleviates diffusion limitations encountered in microporous catalysts such as zeolites, thereby enhancing mass transport properties.[28] Compared to catalysts supported on conventional nanoparticles, mesoporous solid-supported catalysts demonstrate superior catalytic activity, stability, and ease of diffusion, making them highly advantageous for various catalytic applications.

Pyridopyrimidine is an aromatic compound with the formula $C_7H_5N_3$. It is obtained from the coupling of two compounds, pyridine and pyrimidine. The coupling of the pyridopyrimidine ring can be carried out from different parts, each of which exhibits different properties and characteristics. The pyrido[3,2-*d*]pyrimidine compound is one of these heterocycles.[29] Pyridopyrimidine derivatives have a wide range of biological properties such as anti-hypertensive, anti-cancer, anti-viral, and anti-bacterial.[30]

In recent years, the synthesis of pyridopyrimidine derivatives has been reported in the presence of different catalysts such as SBA-15-SO_3H,[31] DIPEAc,[32] MWCNTs@L-His/Cu(II),[33] MNPs-NPBG-SA,[34] and ionic liquids.[35] Although those works report convenient methods, the present method compared with previously reported catalysts has some advantages such as thermal and chemical stability, highly activity, simplicity of procedure, easy reaction work-up, recyclability, clean method and resulting products having high purity.

Today, magnetic nanoparticles are used as catalysts in multicomponent reactions,[36–40] including the Hantzsch reaction, under various conditions.[41–43]

In continuation of our research interest in catalytic reactions,[44–47] in this research, the synthesis of 1,4-dihydropyridine derivatives was explored using barbituric acid, ammonium acetate, and various benzaldehyde derivatives. The reactions were carried out by using a hollow mesoporous magnetic copper ferrite silica functionalized with phosphomolybdic acid as a nanocatalyst in ethanol at 75 °C.

Experimental

General information

The chemicals used in this study were purchased from Fluka and Merck chemical companies and used without further purification. The nanostructures were characterized using a Holland Philips X'Pert powder X-ray diffractometer (XRD) with Cu Kα radiation ($\lambda = 0.154056$ nm), operated at a scanning rate of 2° min^{-1} over a 2θ range of 10° to 100°. Fourier-transform infrared (FT-IR) spectra were recorded using KBr pellets with a PerkinElmer 781 spectrophotometer and a Nicolet Impact 400 FT-IR spectrometer. ^1H NMR spectra were recorded in DMSO-d_6 with a Bruker DRX-400 spectrometer using tetramethylsilane as an internal standard. The morphology of the nanocomposites was examined using scanning electron microscopy (SEM; SIGMA VP). Elemental analysis of the catalyst was carried out by energy-dispersive X-ray spectroscopy (EDX) using an Oxford Instruments system. Magnetic properties of the nanoparticles were measured using vibrating sample magnetometry (VSM; PPMS-9T) at 300 K at Kashan University, Iran. Thermogravimetric analysis (TGA) was performed using a thermal analyser (TGA 1100, Sanaf Electronic Industries). Brunauer–Emmett–Teller (BET) analysis was performed using a Belsorp Mini X. Melting points were determined using a Yanagimoto micro melting point apparatus and are reported uncorrected. The purity of the substrates and the progress of the reactions were monitored by thin-layer chromatography (TLC) on silica gel plates (Polygram SILG/UV 254, Merck).

Catalyst preparation

General procedure for the preparation of $CuFe_2O_4$ nanoparticles. To prepare copper ferrite nanoparticles, 13.5 g (0.05 mol) of iron(III) chloride and 6.04 g (0.025 mol) of copper nitrate were dissolved in 100 mL of double-distilled water. Then, 50 mL of 2 M sodium hydroxide solution was added dropwise to the mixture. The resulting blackish-brown precipitate was stirred magnetically at 80 °C for 2 hours. Subsequently, the precipitate was filtered and washed with double-distilled water. After drying at 80 °C for 6 hours, the product was calcined in a furnace at 500 °C for 4 hours to afford magnetic copper ferrite nanoparticles.

General procedure for preparing the hollow mesoporous silica catalyst. Initially, 0.2 g of copper ferrite nanoparticles and 1.4 g of cetyltrimethylammonium bromide (CTAB) were placed in a beaker, followed by the addition of 320 mL of double-distilled water. The mixture was subjected to ultrasonic treatment for 10 minutes and then transferred into a one-liter round-bottom flask. Subsequently, 440 mL of ethanol was added to the solution, followed by the addition of 2.4 mL of ammonia. Finally, 0.8 mL of tetraethyl orthosilicate (TEOS), previously diluted in 20 mL of ethanol, was added dropwise to the mixture. The resulting solution was stirred magnetically at room temperature for 24 hours. The product was then separated using an external magnetic field (magnet) and washed three times with water and ethanol to ensure purity. The resulting precipitate was dried in an oven at 80 °C for 6 hours.

Functionalization of hollow mesoporous silica with phosphomolybdic acid. To functionalize the hollow mesoporous silica, 0.2 g of copper ferrite-incorporated mesoporous silica and 0.2 g of phosphomolybdic acid were added to a round-bottom flask. Subsequently, 10 mL of absolute ethanol was introduced into the mixture, and the suspension was stirred magnetically at ambient temperature for 18 hours to allow for effective interaction and surface immobilization of the heteropoly acid. Upon completion of the reaction, the resulting catalyst was separated using an external magnetic field, thoroughly washed three times with double-distilled water and ethanol to remove unbound species, and then dried in an oven at 80 °C for 6 hours to ensure complete removal of residual solvents and moisture.

Synthesis of 1,4-dihydropyridine derivatives using a hollow mesoporous silica-coated copper ferrite nanocatalyst functionalized with phosphomolybdic acid. In a 25 mL round-bottom flask, barbituric acid (1 mmol), an appropriate aldehyde derivative (0.5 mmol), ammonium acetate (0.6 mmol), and the synthesized nanocatalyst (30 mg) were added. Ethanol (5 mL) was then introduced into the reaction vessel, and the mixture was stirred at 75 °C using a magnetic stirrer. The progress of the reaction was monitored by TLC. Upon completion, the nanocatalyst was separated from the reaction mixture using an external magnet. The resulting crude product was washed with hot ethanol to obtain a purified compound. The recovered catalyst was washed sequentially with double-distilled water and ethanol, followed by drying in an oven at 80 °C. The dried catalyst was stored for reuse in subsequent reactions.

*5-Phenyl-5,10-dihydropyrido[2,3-d:6,5-d′]dipyrimidine-2,4,6,8-(1H,3H,7H,9H)-tetraone (**4a**).* White solid, m.p. (°C): 303–305, m.p. (°C) rep.: 301–303;[48] IR (KBr) ν (cm^{-1}): 3400 (NH), 2971 (C–H, sp^2 stretch), 1698, 1615 (C=O), 1402, 1513 (C=C, Ar); ^{1}H NMR (DMSO-d_6, 400 MHz) δ (ppm): 10.14 (s, 4H, NH), 7.22 (s, 1H, NH), 7.12 (t, 3H, Ar, $J = 10.1$ Hz), 7.02 (d, 2H, Ar, $J = 7.7$ Hz), 5.92 (s, 1H, CH).

*5-(4-Chlorophenyl)-5,10-dihydropyrido[2,3-d:6,5-d′]dipyrimidine-2,4,6,8-(1H,3H,7H,9H)-tetraone (**4b**).* White solid, m.p. (°C): 295–297, m.p. (°C) rep.: 296–298;[48] IR (KBr) ν (cm^{-1}): 3210 (NH), 2924 (C–H, sp^2 stretch), 1694 (C=O), 1478, 1609 (C=C, Ar); ^{1}H NMR (DMSO-d_6, 400 MHz) δ (ppm): 10.10 (s, 4H, NH), 7.20 (d, 2H, Ar, $J = 8.2$ Hz), 7.10 (s, 1H, NH), 7.02 (d, 2H, Ar, $J = 8.1$).

*5-(4-Nitrophenyl)-5,10-dihydropyrido[2,3-d:6,5-d′]dipyrimidine-2,4,6,8-(1H,3H,7H,9H)-tetraone (**4c**).* White solid, m.p. (°C): 302–304, m.p. (°C) rep.: 298–300;[48] IR (KBr) ν (cm^{-1}): 3398 (NH), 2971 (C–H, sp^2 stretch), 1616 (C=O), 1401 (C=C, Ar); ^{1}H NMR (DMSO-d_6, 400 MHz) δ (ppm): 10.18 (s, 4H, NH), 8.05 (d, 2H, Ar, $J = 8.5$ Hz), 7.22 (d, 2H, Ar, $J = 8.4$ Hz), 7.08 (s, 1H, NH), 6.04 (s, 1H, CH).

*5-(4-Isopropylphenyl)-5,10-dihydropyrido[2,3-d:6,5-d′]dipyrimidine-2,4,6,8-(1H,3H,7H,9H)-tetraone (**4d**).* Orange solid, m.p. (°C): 297–298, m.p. (°C) rep.: 302–304;[48] IR (KBr) ν (cm^{-1}): 3178 (NH), 3033 (C–H, sp^2 stretch), 1653 (C=O), 1495, 1444 (C=C, Ar); ^{1}H NMR (DMSO-d_6, 400 MHz) δ (ppm): 9.98 (s, 4H, NH), 7.25 (s, 1H, NH), 6.68 (d, 2H, Ar, $J = 11.9$ Hz), 6.65 (d, 2H, Ar, $J = 7.9$ Hz), 5.83 (s, 1H, CH), 2.78 (s, 6H).

*5-(3-Nitrophenyl)-5,10-dihydropyrido[2,3-d:6,5-d′]dipyrimidine-2,4,6,8-(1H,3H,7H,9H)-tetraone (**4e**).* White solid, m.p. (°C): 300–302, m.p. (°C) rep.: 297–299;[48] IR (KBr) ν (cm^{-1}): 3224 (NH), 2923 (C–H, sp^2 stretch), 1694, 1622 (C=O), 1515, 1406 (C=C, Ar); ^{1}H NMR (DMSO-d_6, 400 MHz) δ (ppm): 10.18 (s, 4H, NH), 7.93 (d, 1H, Ar, $J = 5.2$ Hz), 7.81 (s, 1H, Ar), 7.47 (d, 2H, CH, $J = 4.6$ Hz), 7.07 (s, 1H, NH), 6.05 (s, 1H, CH).

*5-(4-Bromophenyl)-5,10-dihydropyrido[2,3-d:6,5-d′]dipyrimidine-2,4,6,8-(1H,3H,7H,9H)-tetraone (**4f**).* White solid, m.p. (°C): 304–306, m.p. (°C) rep.: 301–303;[48] IR (KBr) ν (cm^{-1}): 3239 (NH), 2923 (C–H, sp^2 stretch), 1692 (C=O), 1602, 1473 (C=C, Ar); ^{1}H NMR (DMSO-d_6, 400 MHz) δ (ppm): 10.04 (s, 4H, NH), 7.31 (d, 2H, Ar, $J = 8.0$ Hz), 7.02 (s, 1H, NH), 6.95 (d, 2H, Ar, $J = 8.0$ Hz), 5.89 (s, 1H, CH).

*5-(4-Fluorophenyl)-5,10-dihydropyrido[2,3-d:6,5-d′]dipyrimidine-2,4,6,8-(1H,3H,7H,9H)-tetraone (**4g**).* White solid, m.p. (°C): 297–299, m.p. (°C) rep.: 295–297;[48] IR (KBr) ν (cm^{-1}): 3209 (NH), 2932 (C–H, sp^2 stretch), 1688 (C=O), 1602 (C=C, Ar); ^{1}H NMR (DMSO-d_6, 400 MHz) δ (ppm): 10.08 (s, 4H, NH), 7.09 (s, 1H, NH), 6.99 (d, 2H, Ar, $J = 23.1$ Hz), 6.95 (d, 2H, Ar, $J = 8.5$ Hz), 5.89 (s, 1H, CH).

*5-(2,4-Dichlorophenyl)-5,10-dihydropyrido[2,3-d:6,5-d′]dipyrimidine-2,4,6,8-(1H,3H,7H,9H)-tetraone (**4h**).* White solid, m.p. (°C): 285–287, m.p. (°C) rep.: 290–292;[48] IR (KBr) ν (cm^{-1}): 3361 (NH), 3052 (C–H, sp^2 stretch), 1694, 1622 (C=O), 1525, 1401 (C=C, Ar); ^{1}H NMR (DMSO-d_6, 400 MHz) δ (ppm): 10.08 (s, 4H, NH), 7.32 (s, 1H, Ar), 7.23 (d, 2H, Ar, $J = 7.1$ Hz), 7.08 (s, 1H, NH), 5.77 (s, 1H, CH).

*5-(p-Tolyl)-5,10-dihydropyrido[2,3-d:6,5-d′]dipyrimidine-2,4,6,8-(1H,3H,7H,9H)-tetraone (**4i**).* White solid, m.p. (°C): 294–296, m.p. (°C) rep.: 298–300;[48] IR (KBr) ν (cm^{-1}): 3195 (NH), 3001 (C–H, sp^2 stretch), 1612 (C=O), 1402 (C=C, Ar); ^{1}H NMR (DMSO-d_6, 400 MHz) δ (ppm): 10.03 (s, 4H, NH), 7.32 (s, 1H, NH), 6.93 (d, 2H, Ar, $J = 7.9$ Hz), 6.88 (d, 2H, Ar, $J = 7.2$ Hz), 5.87 (s, 1H, CH).

*5-(4-Hydroxyphenyl)-5,10-dihydropyrido[2,3-d:6,5-d′]dipyrimidine-2,4,6,8-(1H,3H,7H,9H)-tetraone (**4j**).* Yellow solid, m.p. (°C): 255–257, m.p. (°C) rep.: 260–262;[48] IR (KBr) ν (cm^{-1}): 3195 (NH), 3001 (C–H, sp^2 stretch), 1612 (C=O), 1402 (C=C, Ar); ^{1}H NMR (DMSO-d_6, 400 MHz) δ (ppm): 10.01 (s, 4H, NH), 8.88 (s, 1H, OH), 7.11 (s, 1H, NH), 6.78 (d, 2H, Ar, $J = 8.1$ Hz), 6.52 (d, 2H, Ar, $J = 8.0$ Hz), 5.80 (s, 1H, CH).

*5-(3-Hydroxyphenyl)-5,10-dihydropyrido[2,3-d:6,5-d′]dipyrimidine-2,4,6,8-(1H,3H,7H,9H)-tetraone (**4k**).* Yellow solid, m.p. (°C): 288–290, m.p. (°C) rep.: 283–285;[48] IR (KBr) ν (cm^{-1}): 3195 (NH), 3001 (C–H, sp^2 stretch), 1612 (C=O), 1402 (C=C, Ar); ^{1}H NMR (DMSO-d_6, 400 MHz) δ (ppm): 10.04 (s, 4H, NH), 8.91 (s, 1H, OH), 7.27 (s, 1H, Ar), 7.09 (s, 1H, NH), 6.97 (d, 1H, Ar, $J = 8.0$ Hz), 6.90 (t, 1H, Ar, $J = 7.4$ Hz), 6.41 (d, 1H, Ar, $J = 8.2$ Hz), 5.84 (s, 1H, CH).

*5-(4-Methoxyphenyl)-5,10-dihydropyrido[2,3-d:6,5-d′]dipyrimidine-2,4,6,8-(1H,3H,7H,9H)-tetraone (**4l**).* Yellow solid, m.p. (°C): 304–306, m.p. (°C) rep.: 300–302;[48] IR (KBr) ν (cm^{-1}): 3195 (NH), 3001 (C–H, sp^2 stretch), 1612 (C=O), 1402 (C=C, Ar); ^{1}H NMR (DMSO-d_6, 400 MHz) δ (ppm): 10.02 (s, 4H, NH), 7.67 (s, 1H, NH), 6.90 (d, 2H, Ar, $J = 8.4$ Hz), 6.70 (d, 2H, Ar, $J = 8.4$ Hz), 5.85 (s, 1H, CH), 3.66 (s, 3H, CH).

Results and discussion

Preparation and characterization of the catalyst

To prepare the catalyst, we have chosen a mixture of $Cu(NO_3)_2$, $FeCl_3$ and NaOH dissolved in deionized water by heating. In the next step, the nano magnetic material in the presence of CTAB was coated with silica. The resulting $CuFe_2O_4$ nanoparticles were then allowed to react under vigorous stirring with an

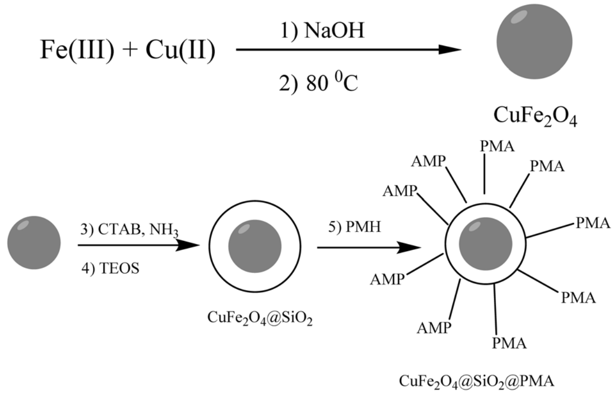

Scheme 1 Preparation of the $CuFe_2O_4@SiO_2@PMA$ nanocatalyst.

appropriate concentration of tetraethyl orthosilicate. Then, the reaction of $CuFe_2O_4@SiO_2$ with phosphomolybdic acid under room temperature condition for 18 h was carried out. The synthetic path for the preparation of the catalyst is shown in Scheme 1. In order to characterize the catalyst structure, the prepared nanocatalyst was analyzed using FT-IR, XRD, SEM, EDX, TGA, BET and VSM techniques.

Fig. 1a–c show the FT-IR spectra of $CuFe_2O_4$ MNPs, $CuFe_2O_4@SiO_2$ and $CuFe_2O_4@SiO_2@PMA$ nanocomposite, respectively. The FT-IR spectrum of $CuFe_2O_4$ MNPs shows peaks characteristic of Cu–O at 431 cm^{-1} and Fe–O 524 cm^{-1} (Fig. 1a). Fig. 1b shows the FT-IR spectrum of $CuFe_2O_4@SiO_2$ MNPs. The bands at 1074 cm^{-1} and 806 cm^{-1} are attributed to the vibration of Si–O–Si bonds (Fig. 1b). Fig. 1c shows the FT-IR spectrum of $CuFe_2O_4@SiO_2@PMA$. The broad band at 3342 cm^{-1} is due to the O–H acidic group. The P–O stretching frequency at 950 cm^{-1} and the Mo–O stretching frequency at 795 cm^{-1} are observed (Fig. 1c).

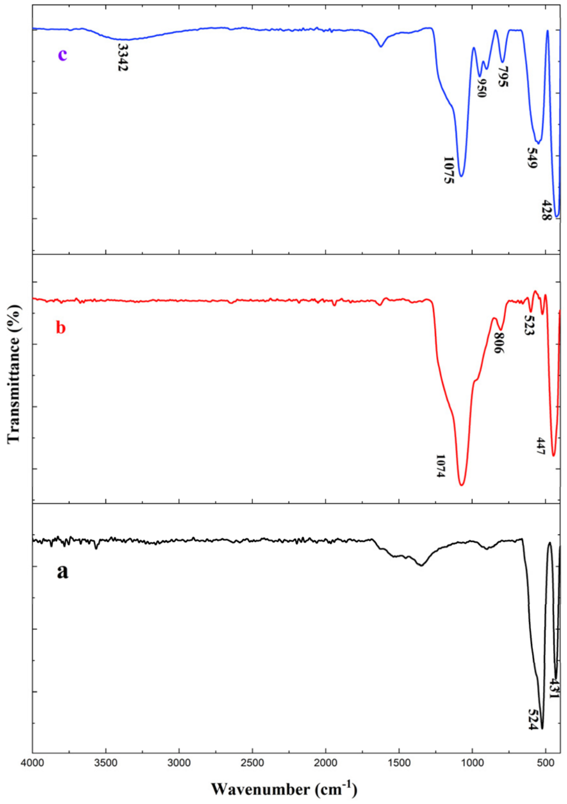

Fig. 1 FT-IR spectra of (a) $CuFe_2O_4$ nanoparticles, (b) $CuFe_2O_4@SiO_2$, and (c) $CuFe_2O_4@SiO_2@PMA$.

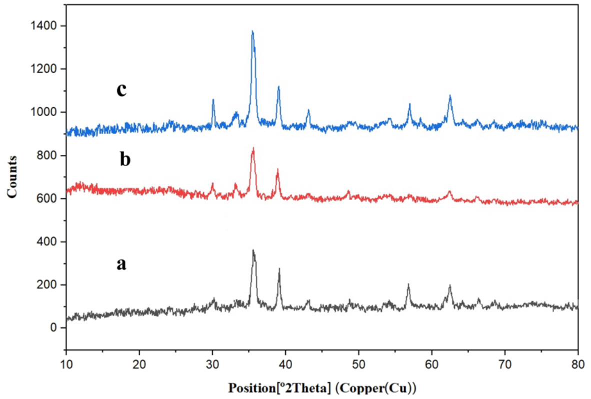

Fig. 2 XRD patterns of (a) $CuFe_2O_4$, (b) $CuFe_2O_4@SiO_2$, and (c) $CuFe_2O_4@SiO_2@PMA$.

The structures of the $CuFe_2O_4$ NPs, $CuFe_2O_4@SiO_2$, and magnetic nanocatalyst were characterized using XRD as shown

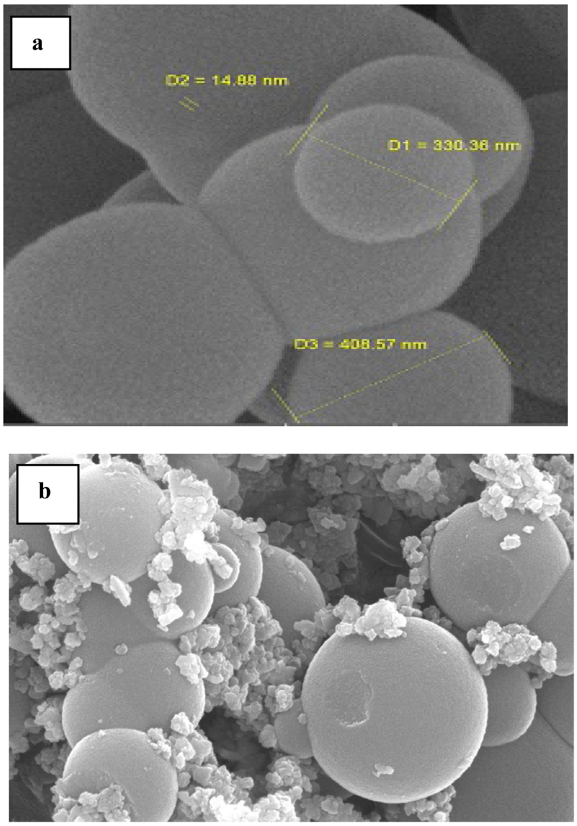

Fig. 3 FE-SEM images of (a) $CuFe_2O_4@SiO_2$ and (b) $CuFe_2O_4@SiO_2@PMA$.

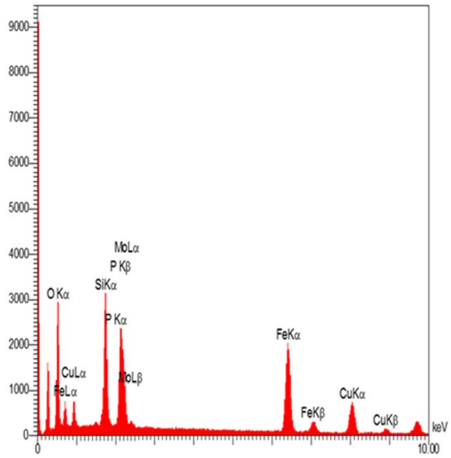

Fig. 4 The EDX pattern of $CuFe_2O_4@SiO_2@PMA$.

Table 1 Concentration of elements in the catalyst

Entry	Element	Atomic%
1	O	58.41
2	Si	23.83
3	P	2.06
4	Mo	2.71
5	Fe	10.37
6	Cu	3.36

in Fig. 2. At 35° were observed the peaks of copper, iron, and molybdenum metals, and the region between 20° and 30° was amorphous, showing a silicate peak. As can be seen in this figure, in the XRD pattern of $CuFe_2O_4$, the crystal peaks for (220), (311), (222), (400), (422), (511) and (440) appeared, indicative of the presence of cubic $CuFe_2O_4$ with $Fd\bar{3}m$ space group (JCPDS card no. 01-077-0010).

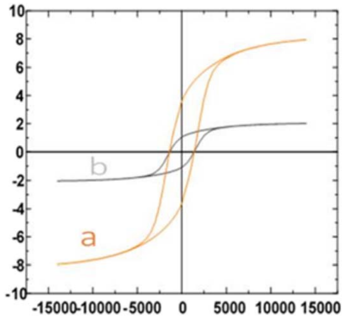

Fig. 6 Magnetization curves for (a) $CuFe_2O_4$ and (b) $CuFe_2O_4@SiO_2@PMA$.

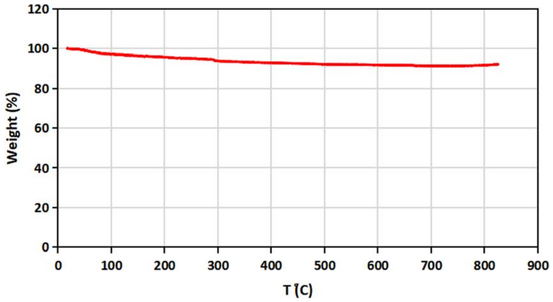

Fig. 7 The TGA curve of $CuFe_2O_4@SiO_2@PMA$.

In order to prove the synthesis of the nanocatalyst, the SEM image of the hollow mesoporous copper ferrite nanocatalyst functionalized with phosphomolybdic acid is shown in Fig. 3 and it shows the changes in the catalyst surface before and after the reaction with phosphomolybdic acid.

Furthermore, the EDX results are shown in Fig. 4, confirming the signals for iron, copper, molybdenum, oxygen, phosphorus,

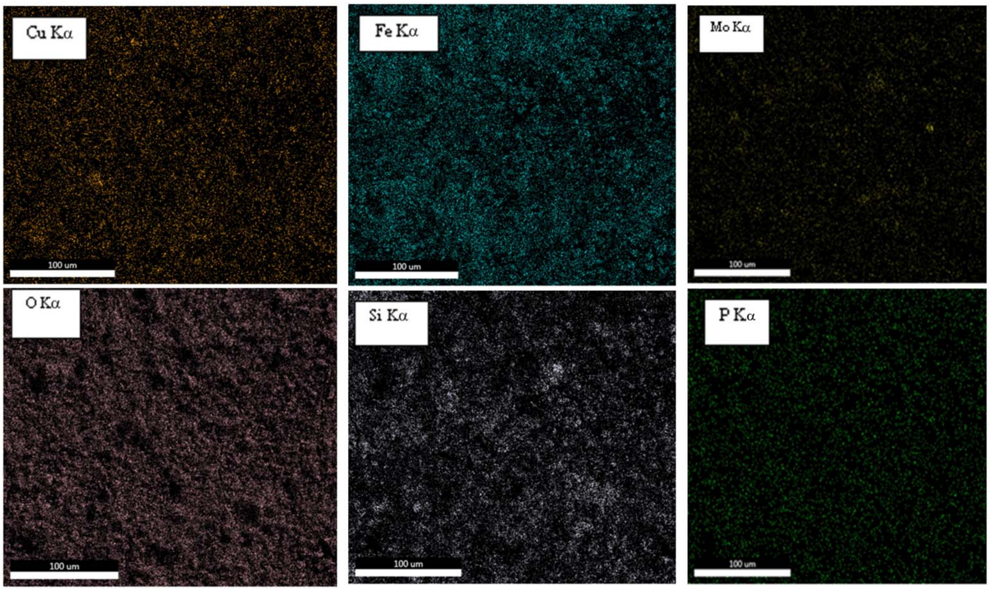

Fig. 5 Elemental mapping of $CuFe_2O_4@SiO_2@PMA$.

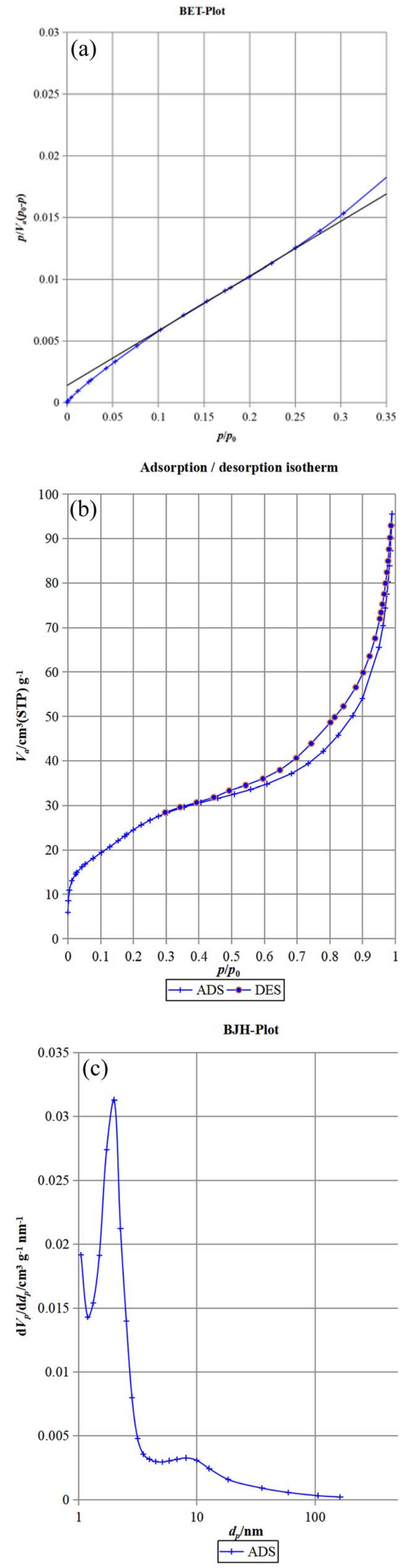

Fig. 8 N_2 adsorption–desorption: (a) BET results for $CuFe_2O_4@SiO_2@PMA$; (b) the isotherm of $CuFe_2O_4@SiO_2@PMA$; and (c) the BJH results for $CuFe_2O_4@SiO_2@PMA$.

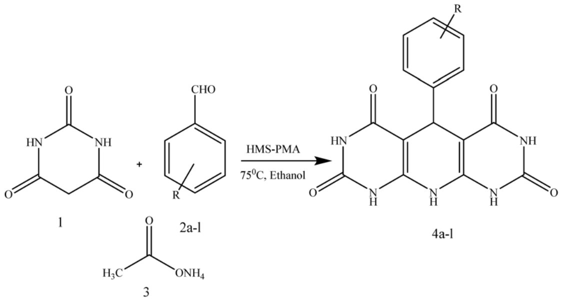

Scheme 2 The synthesis of 5-phenyl-5,10-dihydropyrido[2,3-*d*:6,5-*d*′]dipyrimidine-2,4,6,8-(1*H*,3*H*,7*H*,9*H*)-tetraone using the heterogeneous nanocatalyst.

Table 2 Effects of different amounts of the catalyst on the reaction yield[a]

Entry	Amount of catalyst (g)	Time (min)	Yield[b] (%)
1	0.01	17	65
2	0.02	13	80
3	0.03	10	90
4	0.04	10	90
5	0.05	10	90

[a] Reaction conditions: benzaldehyde (0.5 mmol), barbituric acid (1 mmol), ammonium acetate (0.6 mmol), ethanol as a solvent. [b] Isolated yield.

Table 3 Optimization of the temperature in the presence of the catalyst (0.03 g) in ethanol[a]

Entry	Temp. (°C)	Time (min)	Yield[b] (%)
1	25	30	75
2	40	20	85
3	60	15	87
4	75	10	90
5	80	10	90

[a] Reaction conditions: benzaldehyde (0.5 mmol), barbituric acid (1 mmol), ammonium acetate (0.6 mmol), catalyst (0.03 g), ethanol as a solvent. [b] Isolated yield.

and silicon elements and so indicating the successful synthesis of the nanocatalyst. The results are shown in Table 1, with the presence of Mo: 2.71, Cu: 3.36, Fe: 10.37, P: 2.06, Si: 23.83 and O:

Table 4 Optimization of solvents in the presence of $CuFe_2O_4@SiO_2@PMA$ (0.03 g) under thermal conditions[a]

Entry	Solvent	Time (min)	Yield[b] (%)
1	Water	20	70
2	Methanol	25	76
3	Acetonitrile	50	60
4	Ethanol	10	90
5	Water/ethanol (50%)	15	75

[a] Reaction conditions: benzaldehyde (0.5 mmol), barbituric acid (1 mmol), ammonium acetate (0.6 mmol), catalyst (0.03 g). [b] Isolated yield.

Table 5 The synthesis of 1,4-dihydropyridine derivatives using $CuFe_2O_4@SiO_2@PMA$ as a catalyst under thermal conditions[a]

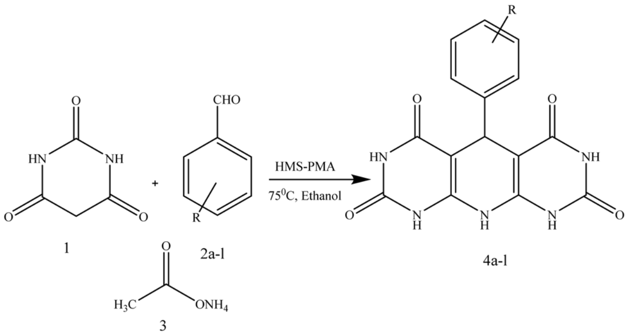

Entry	R	Product	Time (min)	Yield[b] (%)
1	H	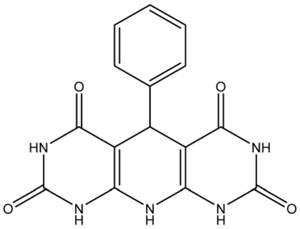	10	90
2	4-Chloro	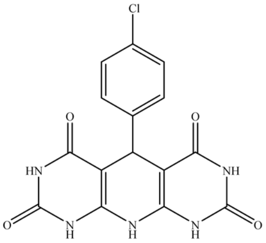	7	95
3	4-Nitro	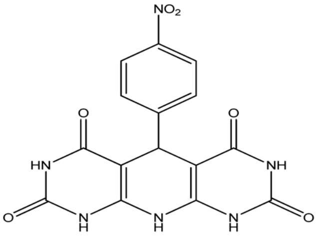	9	92
4	4-Dimethyl	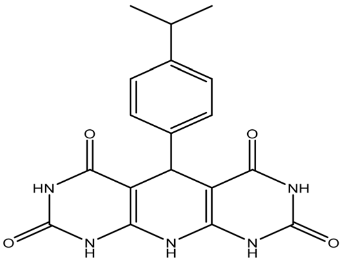	14	85
5	3-Nitro	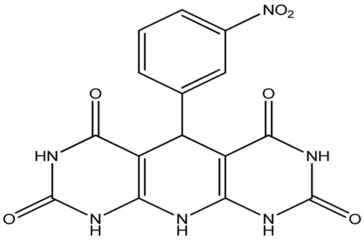	9	90

Table 5 (*Contd.*)

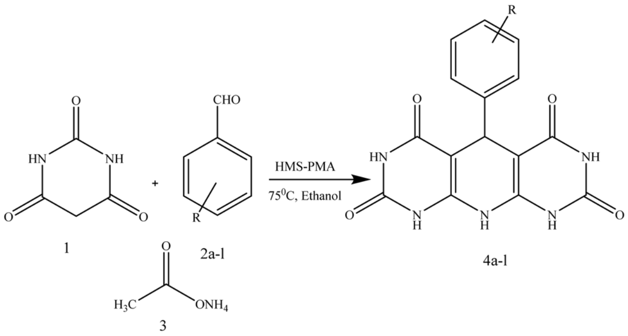

Entry	R	Product	Time (min)	Yield^b (%)
6	4-Bromo	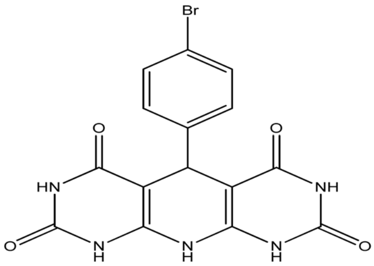	10	94
7	4-Fluoro	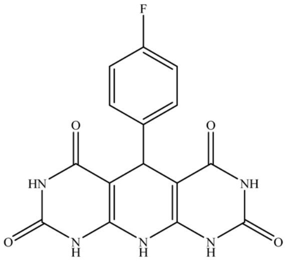	9	90
8	2,4-Dichloro	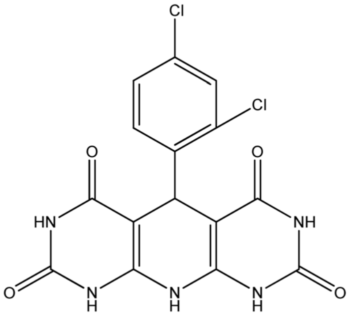	8	93
9	4-Methyl	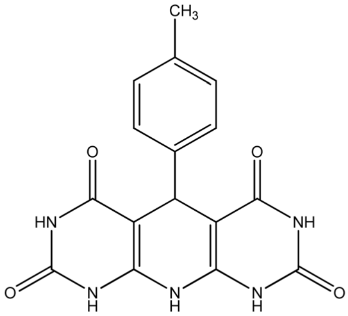	12	80

Table 5 (*Contd.*)

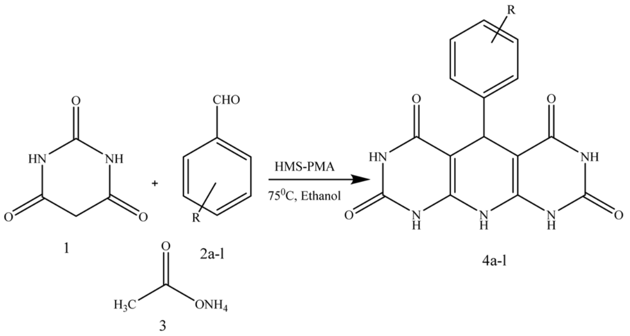

Entry	R	Product	Time (min)	Yield[b] (%)
10	4-Hydroxy	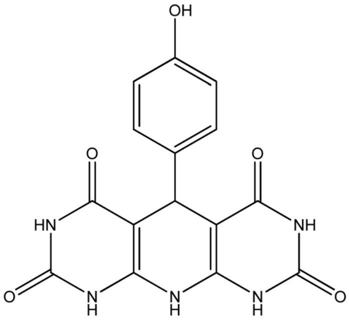	25	80
11	3-Hydroxy	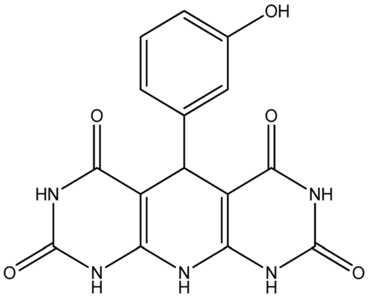	15	85
12	4-Methoxy	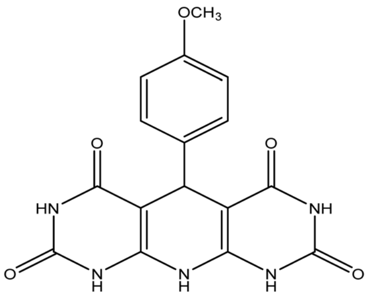	18	75

[a] Reaction conditions: benzaldehyde (0.5 mmol), barbituric acid (1 mmol), ammonium acetate (0.6 mmol), catalyst (0.03 g) under thermal conditions (75 °C) and ethanol as a solvent. [b] Isolated yields.

58.41 in the nanocomposite. Also, a uniform distribution of the elements among the samples, as well as their relative concentration can be seen in the results obtained from the elemental mapping of the samples. Based on the elements present in the $CuFe_2O_4$@SiO_2@PMA nanocatalyst, the mapping images are shown in Fig. 5.

The magnetic properties of $CuFe_2O_4$ nanoparticles and $CuFe_2O_4$@SiO_2@PMA were investigated by the VSM technique at room temperature (Fig. 6). As can be seen, the prepared nanocomposite exhibits paramagnetic behaviour with saturation magnetization of 2.1 emu g^{-1} and for $CuFe_2O_4$ nanoparticles the value is 7.9 emu g^{-1}. This result shows that the saturation magnetization of the sample decreases with functionalization and coating. The reason for the easy separation of $CuFe_2O_4$@SiO_2@PMA as a magnetic nanocatalyst is its high saturation magnetization.

TGA provides valuable information on the thermal stability and the amount of organic and inorganic components of the catalyst. The weight loss stage below 200 °C usually corresponds to the loss of physically adsorbed water and volatile organic solvents. The weight loss between 300 and 800 °C related to the decomposition of organic functional groups confirms the successful functionalization of the nanoparticles with phosphomolybdic acid (Fig. 7).

The N_2 adsorption–desorption isotherms of $CuFe_2O_4$@SiO_2@PMA are shown in Fig. 8. The surface area of $CuFe_2O_4$@SiO_2@PMA is determined as 95.241 $m^2\ g^{-1}$ and the average pore diameter of the catalyst is 5.1765 nm. These results successfully demonstrated the porosity and nanostructure of the catalyst.

Evaluating the catalytic activity of the nanocomposite

In this protocol, the catalytic activity of $CuFe_2O_4$@SiO_2@PMA in the synthesis of chromene compounds was investigated. In order to determine the most appropriate amount of magnetic nanocatalyst, solvent, and temperature for the reaction to obtain the highest efficiency, the reaction of barbituric acid, ammonium acetate and benzaldehyde was treated as a model (Scheme 2). At first, to determine the most suitable catalyst amount in the reaction, different amounts of prepared nanocomposite were used as heterogeneous catalyst in the model reaction under thermal conditions and EtOH solvent. The results are indicated in Table 2.

As can be seen from Table 2, the reaction was efficiently performed using 0.03 g of the catalyst at 75 °C and ethanol as a solvent and the desired product was obtained (Table 2, entry 3).

Then, to optimize the reaction temperature, the reaction was carried out in ethanol at various temperatures (Table 3). The best results were obtained at 75 °C (Table 3, entry 4).

Table 6 Comparison of the current work with previously reported works concerning the synthesis of 1,4-dihydropyridine derivatives

Entry	Product	Time (min)	Yield (%)	Conditions	Ref.
1	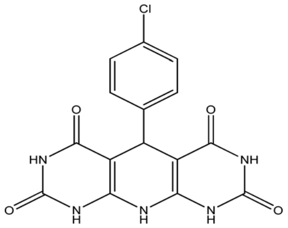	45	92	DIPEAc, RT, solvent free	32
		7	95	$CuFe_2O_4$@SiO_2@PMA, 75 °C, ethanol	This work
2	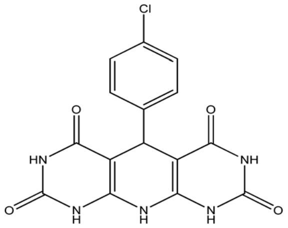	60	95	MWCNTs@L-His/Cu(II), reflux, ethanol	33
		7	95	$CuFe_2O_4$@SiO_2@PMA, 75 °C, ethanol	This work
3	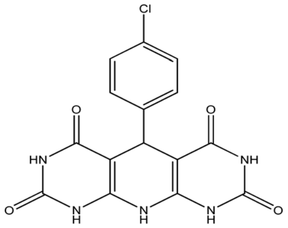	60	88	US, 60 °C, H_2O	49
		7	95	$CuFe_2O_4$@SiO_2@PMA, 75 °C, ethanol	This work
4	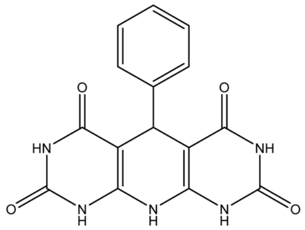	60	87	US, 60 °C, H_2O	49
		10	90	$CuFe_2O_4$@SiO_2@PMA, 75 °C, ethanol	This work

In continuation, the reaction solvent was optimized. The reaction of benzaldehyde (0.5 mmol), barbituric acid (1 mmol), ammonium acetate (0.6 mmol) and $CuFe_2O_4$@SiO_2@PMA (0.03 g) as catalyst under thermal conditions (75 °C) was carried out in various solvents (Table 4). The best results were obtained using ethanol as a solvent (Table 4, entry 4).

Finally after optimization of the reaction conditions, syntheses of 1,4-dihydropyridine derivatives were carried out with the reaction of different aromatic aldehydes including those with electron-withdrawing and electron-donating groups. The corresponding results are depicted in Table 5.

Furthermore, the present work was compared with other previously reported works concerning the synthesis of 1,4-dihydropyridines. The corresponding results are indicated in Table 6. The present method compared with the previously reported ones has some advantages such as high yields, short reaction times, simplicity of procedure, easy reaction work-up, recyclability and resulting products having high purity.

Proposed reaction mechanism for the synthesis of 1,4-dihydropyridine derivatives

The proposed reaction mechanism for the synthesis of 1,4-dihydropyridines involves the reaction of barbituric acid, aromatic aldehydes, and ammonium acetate in the presence of the $CuFe_2O_4$@SiO_2@PMA catalyst as illustrated in Scheme 3. Initially, the carbonyl group of the benzaldehyde is activated by the catalyst resulting in a reduction of the electron density on the carbonyl carbon, making it more susceptible to nucleophilic attack. Then, the Knoevenagel condensation reaction between the activated aldehyde and barbituric acid gives compound **I**.

Simultaneously with this reaction, ammonia reacts with another barbituric acid and creates enamine compound **II**. In the next step, a Michael-type addition of compound **II** to compound **I** and tautomerization lead to intermediate **III**. The product is formed by intramolecular attack of the amino group onto the activated carbonyl group in intermediate **III**. This

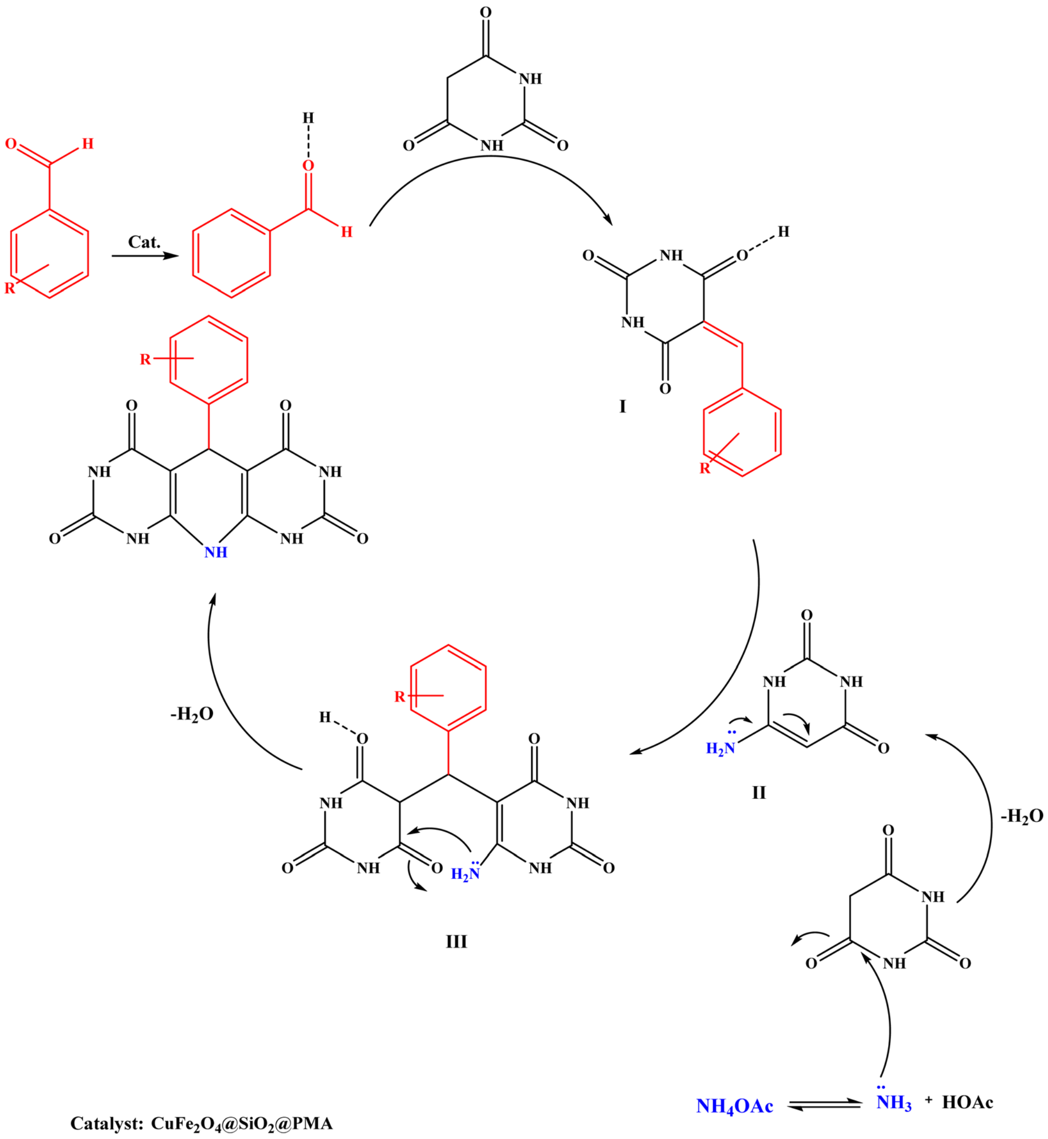

Scheme 3 The proposed reaction mechanism for the synthesis of 1,4-dihydropyridine derivatives with $CuFe_2O_4$@SiO_2@PMA as catalyst.

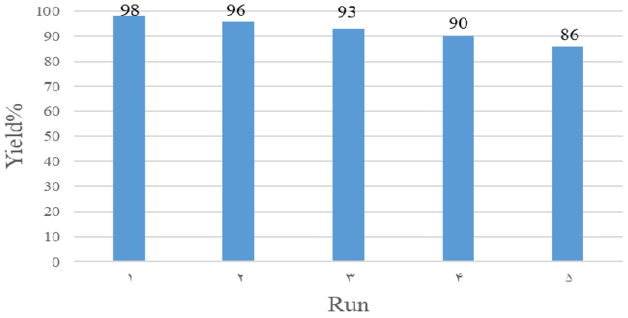

Fig. 9 The reusability of the $CuFe_2O_4$@SiO_2@PMA catalyst.

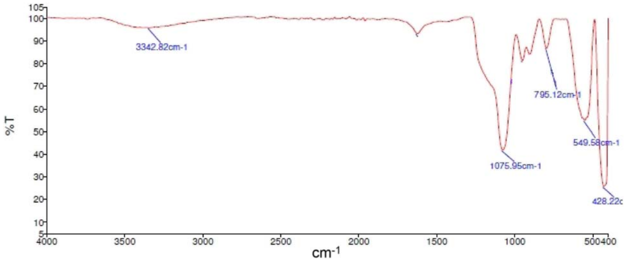

Fig. 10 The FT-IR spectrum of the reused catalyst.

process is followed by cyclization and dehydration to produce 1,4-dihydropyridine compounds.[50]

Catalyst reusability

After the completion of the reaction, the heterogeneous catalyst was separated from the reaction mixture using an external magnet. Following its separation, it was washed with ethyl acetate to remove any remaining organic compounds. Then, the recovered catalyst was dried in an oven at 50 °C and reused in the model reaction. Fig. 9 shows its catalytic activity for five cycles. Furthermore, to prove the stability and performance of the recovered nanocatalyst, the recovered catalyst was analyzed using FT-IR, XRD and FE-SEM methods. As seen, there is no significant difference between the FT-IR, XRD and FE-SEM analyses of the initial and recovered nanocomposite (Fig. 10–12). To test the heterogeneous nature of the catalyst, a hot filtration test was carried out for the synthesis of **4j** product under optimum reaction conditions. After 15 min of the reaction, the catalyst was separated from the reaction mixture using an external magnet and then the filtrate was allowed to react further for the other half of the reaction time. The results showed no further product after the separation of the catalyst, and thus the catalyst acts heterogeneously in the reaction media without any leaching of its active sites.

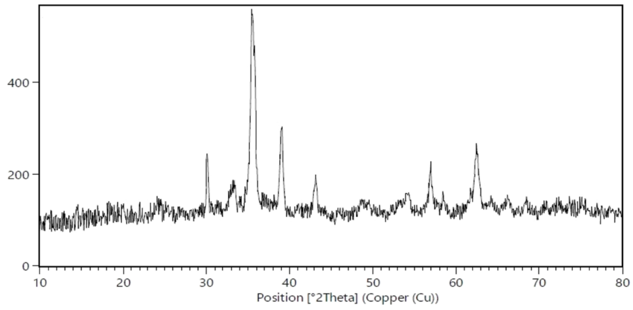

Fig. 11 The XRD pattern of the reused catalyst.

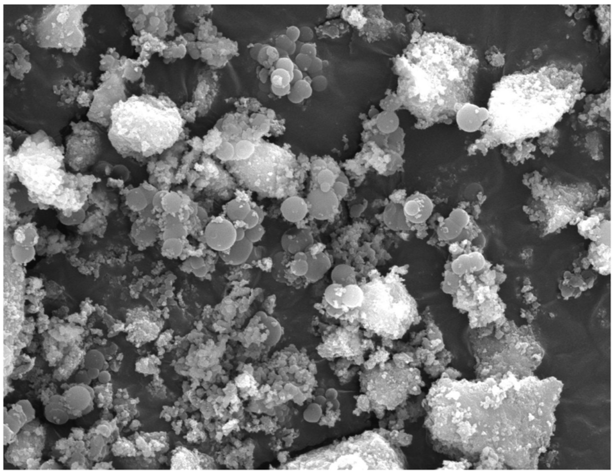

Fig. 12 An FESEM image of reused $CuFe_2O_4$@SiO_2@PMA catalyst.

Conclusions

In this research, different compounds of dihydropyrido derivatives were synthesized. The synthesis of these derivatives was carried out under mild conditions and in the presence of a hollow mesoporous nanocomposite. This nanocomposite was prepared and identified as an efficient catalyst for the one-pot synthesis of 1,4-dihydropyridine derivatives under clean and mild reaction conditions. High yields, short reaction times, environmental friendliness, reusability and the easy recovery of the catalyst using an external magnet are the important features of this methodology. The products were identified based on physical and spectroscopic data, such as melting point, FT-IR and ^1H NMR analyses. Also, the catalyst was characterized using FT-IR, XRD, EDX, SEM, TGA, BET and VSM techniques.

Conflicts of interest

There are no conflicts to declare.

Data availability

The datasets generated and analyzed during the current study are available from the Hossein Naeimi repository (naeimi@kashanu.ac.ir).

Supplementary information (SI): FT-IR and ^1H NMR spectra. See DOI: https://doi.org/10.1039/d5ra06191a.

Acknowledgements

The authors are grateful to University of Kashan for supporting this work through grant no. 159148/86.

References

1 M. Fan, J. Yan, H. Tan, Y. Miao and X. Hu, *J. Mater. Chem. B*, 2014, **2**, 8399–8405.
2 B. Gleich, C. Rümenapp and A. Haase, *Pharm. Res.*, 2012, **29**, 1165–1179.
3 Z. Zhou, L. Yang, J. Gao and X. Chen, *Adv. Mater.*, 2019, **31**, 1804567.
4 N. A. Frey, S. Peng, K. Cheng and S. Sun, *Chem. Soc. Rev.*, 2009, **38**, 2532–2542.
5 L. Gloag, M. Mehdipour, D. Chen, R. D. Tilley and J. J. Gooding, *Adv. Mater.*, 2019, **31**, 1904385.
6 S. Nikazar, M. Barani, A. Rahdar, M. Zoghi and G. Z. Kyzas, *ChemistrySelect*, 2020, **5**, 12590.
7 L. Arda, N. Dogan and C. Boyraz, *J. Supercond. Novel Magn.*, 2018, **31**, 365.
8 M. K. Satheeshkumar, E. R. Kumar, P. Indhumathi, C. Srinivas, M. Deepty, S. Sathiyaraj, N. Suriyanarayanan and D. L. Sastry, *Inorg. Chem. Commun.*, 2020, **111**, 107578.
9 S. M. Rathod, A. R. Chavan, S. S. Jadhav, K. M. Batoo, M. Hadi and E. H. Raslan, *Chem. Phys. Lett.*, 2021, **765**, 138308.
10 F. Sharifianjazi, M. Moradi, N. Parvin, A. Nemati, A. J. Rad, N. Sheysi, A. Abouchenari, A. Mohammadi, S. Karbasi, Z. Ahmadi, A. Esmaeilkhanian, M. Irani, A. Pakseresht, S. Sahmani and M. S. Asl, *Ceram. Int.*, 2020, **46**, 18391.
11 Y. J. Yang, C. Jiang, S. Chen, N. Wang, P. Yang, M. Liu and Y. Cheng, *J. Electroanal. Chem.*, 2022, **918**, 116385.
12 K. Shahzad, S. Mushtaq, M. Rizwan, W. Khalid, M. Atif, F. Din Ud, N. Ahmad, R. Abbasi and Z. Ali, *Mater. Sci. Eng., C*, 2021, **119**, 111444.
13 R. A. Raimundo, V. D. Silva, L. S. Ferreira, F. J. A. Loureiro, D. P. Fagg, D. A. Macedo, U. U. Gomes, R. M. Gomes, M. M. Soares and M. A. Morales, *J. Alloys Compd.*, 2023, **940**, 168783.
14 S. Kumar, A. Ohlan, P. Kumar and V. Verma, *J. Supercond. Novel Magn.*, 2020, **33**, 1187.
15 A. A. Al-Juaid, *Mater. Res. Express*, 2023, **10**, 026101.
16 B. Yalcin, *J. Nanopart. Res.*, 2022, **24**, 271.
17 M. Chithra, C. N. Anumol, V. Argish, B. N. Sahu and S. C. Sahoo, *Mater. Sci.*, 2023, **34**, 806.
18 G. A. Lone and M. Ikram, *J. Alloys Compd.*, 2023, **934**, 167891.
19 D. H. Everett, *Pure Appl. Chem.*, 1972, **31**, 577–638.
20 H. Zheng, F. Gao and V. Valtchev, *J. Mater. Chem. A*, 2016, **4**, 16756–16770.
21 X. Du and J. He, *Langmuir*, 2010, **26**, 10057–10062.
22 A. B. D. Nandiyanto, A. Suhendi, T. Ogi, T. Iwaki and K. Okuyama, *Colloids Surf., A*, 2012, **396**, 96–105.
23 C. Yu, B. Tian, J. Fan, G. D. Stucky and D. Zhao, *Chem. Commun.*, 2001, 2726–2727.
24 T. Asefa and Z. Tao, *Can. J. Chem.*, 2012, **90**, 1015–1031.
25 M. A. Balestriere, K. Schuhladen, K. H. Seitz, A. R. Boccaccini, S. M. Cere and J. Ballarre, *J. Electroanal. Chem.*, 2020, **876**, 114735.
26 W. Zhang, H. He, Y. Tian, K. Lan, Q. Liu, C. Wang, Y. Liu, A. Elzatahry, R. Che, W. Li and D. Zhao, *Chem. Sci.*, 2019, **10**, 1664–1670.
27 X. Lu, G. Hasegawa, K. Kanamori and K. Nakanishi, *J. Sol-Gel Sci. Technol.*, 2020, 1–21.
28 Y. Wu, W. Zhao, Y. Qiang, Z. Chen, L. Wang, X. Gao and Z. Fang, *Carbon*, 2020, **159**, 292–302.
29 M. Jang, *Synthesis and Biological Evaluation of Bicyclic Heterocycles*, 2009, pp. 1–150.
30 T. Mohamed, M. K. Mann and P. P. N. Rao, *RSC Adv.*, 2017, **736**, 22360–22368.
31 S. Rostamizadeh, L. Tahershamsi and N. Zekri, *J. Iran. Chem. Soc.*, 2015, **12**, 1381–1389.
32 M. R. Bhosle, L. D. Khillare, J. R. Mali, A. P. Sarkate, D. K. Lokwani and S. V. Tiwari, *New J. Chem.*, 2018, **42**, 18621–18632.
33 H. Saeidiroshan and L. Moradi, *J. Organomet. Chem.*, 2019, **893**, 1–10.
34 D. M. Gholami, N. Foroughifar, A. Khajeh-Amiri and H. N. Pasdar, *J. Chin. Chem. Soc.*, 2018, **65**, 1356–1369.
35 H. Naeimi, A. Didar, Z. Rashid and Z. Zahraie, *J. Antibiot.*, 2017, **70**, 845–852.
36 H. Singh, A. Kachore, V. Aggarwal, E. Bala, Saima, R. Kumar, P. Kumar and P. K. Verma, *ChemistrySelect*, 2025, **10**, e202501004.
37 H. Singh, A. Kachore, V. Aggarwal, E. Bala, Saima, M. Selvaraj and P. K. Verma, *Chem. Rec.*, 2025, **25**, e202500069.
38 E. Bala, A. Kachore, V. Aggarwal, H. Singh, Saima, M. Selvaraj, R. Kumar and P. K. Verma, *JPhys Mater.*, 2025, **708**, 135961.
39 A. Kachore, E. Bala, V. Aggarwal, H. Singh, Saima, M. H. Adam Suleiman, M. Selvaraj and P. K. Verma, *J. Ind. Eng. Chem.*, 2025, **146**, 494–505.
40 V. Aggarwal, A. Kachore, E. Bala, H. Singh, M. Selvaraj, M. A. Assiri, Saima, R. Kumar and P. K. Verma, *J. Phys. Chem. Solids*, 2026, **208**, 113060.
41 V. Aggarwal, A. Kachore, E. Bala, H. Singh, M. Selvaraj, M. A. Assiri, Saima, R. Kumar, R. Sharma and P. K. Verma, *J. Taiwan Inst. Chem. Eng.*, 2025, **175**, 106249.
42 H. Singh, Himanshu, A. Kachore, V. Aggarwal, E. Bala, Saima, R. Kumar and P. K. Verma, *Langmuir*, 2025, **41**, 23163–23181.
43 G. Lavanya, S. A. Khadar, I. Jariya, M. Sasikala, V. Kalpana, A. Padmanaban, J. Wang and B. M. Ali, *ChemistrySelect*, 2024, **9**, e202403664.
44 M. Dadaei and H. Naeimi, *RSC Adv.*, 2021, **11**, 15360.
45 H. Naeimi and M. Dadaei, *RSC Adv.*, 2015, **5**, 76221.
46 M. Ansari, A. H. Ghasemi and H. Naeimi, *RSC Adv.*, 2025, **15**, 18535–18547.
47 H. Hassanpour and H. Naeimi, *RSC Adv.*, 2024, **14**, 17296–17305.
48 D. M. Gholami, N. Foroughifar, A. Khajeh-Amiri and H. N. Pasdar, *J. Chin. Chem. Soc.*, 2018, **65**, 1356–1369.
49 M. H. Mosslemin and M. R. Nateghi, *Ultrason. Sonochem.*, 2010, **17**, 162–167.
50 H. Naeimi and A. Didar, *Ultrason. Sonochem.*, 2017, **34**, 889–895.